Tight-binding model for semiconductor quantum dots with a wurtzite crystal structure: From one-particle properties to Coulomb correlations and optical spectra

S. Schulz, S. Schumacher, and G. Czycholl
Institute for Theoretical Physics, University of Bremen, 28359 Bremen, Germany
(Received 22 December 2005; revised manuscript received 24 March 2006; published 22 June 2006)

In this work we investigate the electronic and optical properties of self-assembled quantum dots by means of a tight-binding model. Coulomb and dipole matrix elements are calculated from the one-particle wave functions which fully include the atomistic wurtzite structure of the low-dimensional heterostructures and serve as an input for the calculation of optical spectra. For the investigated InN/GaN material system, the optical selection rules are found to be strongly affected by band-mixing effects for the localized valence band states. Within this framework, excitonic absorption and emission spectra are analyzed for different sizes of the investigated lens-shaped quantum dots, including the influence of the intrinsic and strain-induced electrostatic field of the wurtzite structure. A dark exciton ground state for small quantum dots is found.

DOI: 10.1103/PhysRevB.73.245327 PACS number(s): 78.67.Hc, 73.22.Dj, 71.35.−y

I. INTRODUCTION

Semiconductor quantum dots (QDs) are subject of intense experimental and theoretical research.[1] As a new material system, group-III nitrides are of particular interest due to their wide range of emission frequencies from red to ultraviolet.[2,3] As a technologically promising manifestation of zero-dimensional heterostructures we study self-assembled QDs, which can typically be grown by molecular beam epitaxy in Stranski-Krastanov growth mode.

For the description of the electronic properties of these low-dimensional heterostructures a variety of different theoretical approaches is available. Starting with models, which are based on a continuumlike description of the crystal structure, there are effective-mass[4,5] and $k\cdot p$ (Refs. 6–8) approaches. These models represent a description on a macroscopic level and can be used instead of a more complicated and numerically expensive atomistic description. The fundamental electronic properties are included via effective-mass or Luttinger parameters, respectively, to reproduce important features of the bulk band structure. The applicability of one-component effective mass theories is limited to model studies or situations where band-mixing effects are of minor importance. A $k\cdot p$ formulation provides a more sophisticated approach, where band-mixing effects can be studied[6] and where important symmetry properties of the underlying crystal lattice and of the QD geometry can be included.

However, to understand all features of the electronic spectra of low-dimensional heterostructures, an atomistic treatment becomes necessary as has recently been demonstrated in Ref. 9. On the atomistic level, different approaches have successfully been applied in the past, namely the empirical pseudopotential method,[10–12] tight-binding (TB) models,[13–15] and atomic bond-orbital models,[16] which all include the atomistic crystal structure and provide a multiband description of the complicated valence band structure. Being the least commonly used atomistic approach, the atomic bond-orbital model can be characterized to be situated somewhere in between the TB and typical $k\cdot p$ models.[17,18]

The above-mentioned approaches have extensively been applied to study the electronic and optical properties of a variety of different heterostructures where most commonly QD (Refs. 11 and 14–16) and quantum well[13,19,20] (QW) systems have been studied. Some of the semiconductor materials of interest, e.g., InAs, GaAs, CdSe, crystallize in the zinc-blende structure, whereas some are also available with a wurtzite crystal structure, e.g., CdSe, and some are almost exclusively found with a wurtzite structure, e.g., ZnO, InN, GaN, AlN. Whereas for the zinc-blende structure the influence of atomistic effects has previously been studied and recently been emphasized again,[9] for the wurtzite structure comparatively little theoretical information is available and there are certain aspects that have not been addressed on an atomistic level in great detail.

Amongst the wurtzite semiconductors, especially the technologically interesting group-III nitrides have recently attracted considerable attention. Quite a lot theoretical[21,22] and experimental[23,24] information is available concerning GaN/AlN QD systems[21–24] with emitting wavelengths in the blue or ultraviolet region. So far, much less effort has been spent on InN/GaN QDs which are of current interest to extend the emission wavelength of group-III nitride structures to the red and infrared spectral region.[25] So far, most of the theoretical work concerning InN QD structures is based on effective-mass[26,27] and $k\cdot p$ calculations.[28]

To provide further valuable insight into the nature of III-nitride QDs, we investigate the optical properties of self-assembled InN/GaN quantum dots on an atomistic level by means of a TB formulation. We focus our attention on small QDs in order to minimize the quantum confined Stark effect (QCSE) which reduces the light emitting efficiency of larger nitride-based QDs and therefore limits their applicability for optoelectronic devices.[29,30] We show how Coulomb and dipole matrix elements can be calculated and investigate the influence of the wurtzite crystal structure, of band-mixing effects for the localized hole states, and of the built-in (spontaneous and strain-induced) electrostatic field. For the calculation of the dipole matrix elements we introduce numerically orthogonalized Slater orbitals, which fulfill all basic requirements for calculations in terms of an orthogonal empirical TB model. Furthermore, we discuss the influence of the specific choice of localized orbitals as has been done in

Refs. 31 and 32 for Coulomb matrix elements before.

The calculation of Coulomb and dipole matrix elements between the microscopically determined one-particle QD states allows to investigate excitonic spectra by means of a full configuration-interaction (FCI) approach[33–36] with atomistically determined input parameters.

As a basic result, it is shown by our investigation that for small lens-shaped InN/GaN QDs the exciton ground state emission vanishes. For larger QDs the twofold degenerate p-like states constitute the hole ground states, which have nonvanishing dipole matrix elements with the electron ground state. This is in agreement with recent $k\cdot p$ calculations[28] and experiments for CdSe QDs.[37] However, although this leads to an—in principle—bright ground state exciton emission for larger QDs, the QCSE, induced by the built-in field, reduces the oscillator strengths by more than one order of magnitude. In the smaller QDs the spatial separation of electron and hole wave functions by the QCSE can drastically be reduced, but the ground state becomes completely dark since the lowest hole states are interchanged.

II. THE TIGHT-BINDING MODEL

We use a TB model with an sp^3 basis $|\alpha,\mathbf{R}\rangle$, i.e., one s state ($\alpha=s$) and three p-states ($\alpha=p_x,p_y,p_z$) per spin direction at each atom site $\mathbf{R}$. In this basis set the TB matrix elements are given by

$$E_{\alpha\mathbf{R},\alpha'\mathbf{R}'}=\langle\alpha\mathbf{R}|H^{\text{bulk}}|\alpha'\mathbf{R}'\rangle. \tag{1}$$

The indices $\mathbf{R}$ and α label the lattice sites and the different types of orbitals, respectively. We include nondiagonal elements of the TB Hamiltonian matrix up to nearest neighbors and use the two-center approximation of Slater and Koster[39] which yields nine independent TB parameters. In contrast to most other III-V and II-VI semiconductors, one can neglect spin-orbit coupling and crystal-field splitting in InN and GaN which are of the order of $\sim$10 meV.[3,40] In accordance with the small crystal field splitting we treat the four nearest neighbors of each atom as being equivalent.

The electronic properties of the pure bulk materials are given in $\mathbf{k}$ space by a 16×16 matrix $\underline{\underline{H}}^{\text{bulk}}(\mathbf{k})$ for each $\mathbf{k}$ point, with the basis states $|\mathbf{k}\alpha\rangle$.[38] This matrix depends on the different TB parameters $E_{\alpha\mathbf{R},\alpha'\mathbf{R}'}$. These parameters are empirically determined such that the characteristic properties of the bulk band structure—as known from experiment and band structure calculations[41,42]—in the vicinity of the Γ point are reproduced. For the wurtzite structure this procedure roughly corresponds to a simultaneous fit at the Γ and L symmetry points in the zinc-blende structure.[43] The resulting TB band structures are depicted in Fig. 1 and the parameters are given in Table I [the general notation of Eq. (1) is specialized for the system investigated here following Ref. 38]. Comparing with the literature,[41,42] the complicated valence band structure is excellently reproduced over the Brillouin zone whereas the s-like conduction band is best reproduced in the vicinity of the Γ point. For the GaN we obtain effective electron masses along the z axis of $m_{\parallel}=0.259m_0$ and along the x axis of $m_{\perp}=0.256m_0$. These values are in good agreement with the experimentally observed ones of $m_{\parallel}=(0.228\pm0.008)m_0$ and $m_{\perp}=(0.237\pm0.006)m_0$ by Kasic *et al.*[44] For the InN, we obtain an isotropic effective mass $m=m_{\parallel}=m_{\perp}=0.069m_0$. This value is in excellent agreement with the literature value[3,45] of $m=0.07m_0$. In principle, the conduction band structure can be improved by taking into account more basis states per unit cell.[46] However, for the discussion of the optical properties of the investigated materials, an appropriate description of the electronic structure in the region near the Γ point is sufficient. Therefore, the sp^3 TB model is satisfactory for our purposes, namely the calculation of optical properties for InN/GaN QDs.

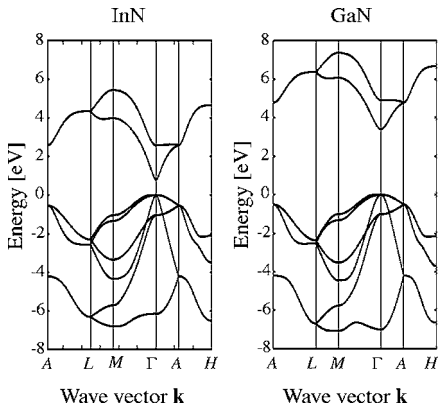

FIG. 1. Tight-binding band structure for bulk InN and GaN. The corresponding tight-binding parameters for each material are given in Table I.

III. THE QUANTUM DOT

Starting from the bulk TB parameters, the QD is modeled on an atomistic level. Within the restricted basis set, the resulting ith TB wave function $\psi_i(\mathbf{r})$ can be expressed in terms of the localized orbitals $\phi_{\alpha\mathbf{R}}(\mathbf{r})=\langle\mathbf{r}|\alpha,\mathbf{R}\rangle$ at lattice site $\mathbf{R}$ with the TB coefficients $c^i_{\mathbf{R}\alpha}$,

$$\psi_i(\mathbf{r})=\sum_{\mathbf{R}\alpha}c^i_{\mathbf{R}\alpha}\phi_{\alpha\mathbf{R}}(\mathbf{r}). \tag{2}$$

The Schrödinger equation leads to a matrix eigenvalue problem with finite dimension,

TABLE I. Tight-binding parameters for the nearest neighbors of wurtzite InN and GaN. The notation of Ref. 38 is used.

	InN (eV)	GaN (eV)
$E(s,a)$	−6.791	−11.012
$E(p,a)$	0.000	0.005
$E(s,c)$	−3.015	1.438
$E(p,c)$	8.822	10.896
$V(s,s)$	−5.371	−5.318
$V(x,x)$	0.022	−0.222
$V(x,y)$	6.373	7.136
$V(sa,pc)$	0.370	0.628
$V(pa,sc)$	7.5	7.279

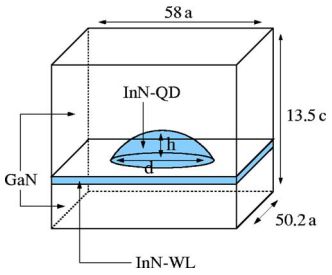

FIG. 2. (Color online) Illustration of the finite-size supercell in which the QD geometry is modeled. The investigated lens-shaped InN QDs are sitting atop of an InN wetting layer (WL) and have circular symmetry around the z axis. The InN QD-WL system is embedded in a GaN matrix.

$$\sum_{\mathbf{R}\alpha} \langle \alpha' \mathbf{R}' | H | \alpha, \mathbf{R} \rangle c^i_{\mathbf{R}\alpha} - E^i c^i_{\mathbf{R}'\alpha'} = 0, \tag{3}$$

where E^i is the corresponding energy eigenvalue. For the matrix elements $\langle \alpha' \mathbf{R}' | H | \alpha, \mathbf{R} \rangle$ we use the TB parameters of the bulk materials, which are given in Sec. II.

To model an InN QD embedded in a GaN matrix, a finite wurtzite lattice within a cell with fixed boundary conditions is chosen. With fixed boundary conditions no artificial dot-dot coupling occurs, which can be the case with periodic boundary conditions.[14,21] However, a sufficiently large supercell is required in order to avoid numerical artifacts in the localized QD states, especially artifacts due to the cubic symmetry of the boundaries. Surface effects in the finite-size supercell are removed according to the guidelines given in Ref. 47. The parameters for each site are set according to the occupying atoms (N, In, Ga) in the InN/GaN heterostructure. At the InN/GaN interfaces averages of the TB parameters are used[48] to take into account that the nitrogen atoms cannot unambiguously be attributed to the InN or the GaN material, respectively. The valence band offset ΔE between the two materials (InN and GaN) is included in our model by shifting the diagonal matrix elements of the bulk InN. In the past, several different values for the InN/GaN valence band offset have been reported. The theoretically calculated values, e.g., 0.3 eV (Ref. 49) and 0.48 eV,[40] are relatively small compared with the experimentally obtained ones of (1.05 ± 0.25) eV (Ref. 50) or (1.26 ± 0.23) eV.[51] A detailed discussion of this issue is given by Vurgaftman *et al.* in Ref. 3. We chose a valence band offset of $\Delta E = 0.5$ eV, as recommended by Vurgaftman *et al.* A different value would affect the strengths of the confinement potentials for electrons and holes inside the QD structure. As a consequence the QD states might be slightly shifted in energy. However, no qualitative changes of our results are expected since only well localized states are investigated here.

We consider lens-shaped InN QDs, grown in (0001)-direction on top of an InN wetting layer (WL). The embedded QD-WL system is schematically shown in Fig. 2. For the WL we assume a thickness of one lattice constant c. The rotational symmetry of the QD system around the z axis preserves the intrinsic C_{3v} symmetry of the underlying wurtzite crystal which is important for the discussion of one-particle properties and Coulomb correlations. This is in contrast to the recent discussion on self-assembled QDs with a zinc-blende crystal structure in Ref. 9, where the C_{4v} symmetry of the QD geometry is spoiled by the symmetry of the underlying atomistic lattice. Since the inversion is not a symmetry operation for typical self-assembled QD structures, the overall system symmetry is then reduced to a C_{2v} symmetry. This reduction in symmetry results in an additional splitting of otherwise degenerate one-particle energy levels in the structure.[9,15]

In order to give a representative overview of one-particle and excitonic (optical) properties, we study three different QD sizes with diameters $d = 4.5, 5.7, 7.7$ nm and heights $h = 1.6, 2.3, 3.0$ nm, respectively. For all three QD sizes a supercell with the dimension $58a \times 50.2a \times 13.5c$ (188 181 atoms) is used in our calculations to reach good convergence for the localized QD states.

The lattice mismatch between InN and GaN leads to the occurrence of a strain field in the heterostructure. This field modifies the conduction- and valence-band edge of the InN QD. Fonseca *et al.*[52] compared the electronic structure of coupled InAs/GaAs QDs for the case when the strain field is included from a microscopic calculation with the case when the strain field is modeled by a constant band-edge shift. The results for the bound electron states with inclusion of the exact strain field do not significantly differ from the results obtained with a constant band shift. However, the influence of the strain effects on the valence-band structure is more complicated. For example, in the well-studied zinc-blende structure, the possible splitting of light- and heavy-hole bands depends on the sign and magnitude of the biaxial strain,[53] and will therefore vary from system to system. In the present work we deal with an InN QD with an underlying wurtzite crystal structure for which comparable studies are rare. For this reason, we compare the bound single-particle wave functions obtained from our TB model with those of $k \cdot p$ calculations, including the strain on a microscopic level, by Andreev *et al.*[21] and Fonoberov *et al.*[54] for similar QD systems (truncated hexagonal pyramidal GaN/AlN QDs). As we will discuss in Sec. III B, our results agree very well with these previous results. Therefore, only slight changes of the one-particle states and energy levels are expected from an additional microscopic inclusion of strain effects in our model. Since we are interested in more general aspects, we neglect the influence of strain-induced displacements from the ideal atom positions, which will be investigated in the future. For the chosen QD geometry strain-induced displacements do not change the symmetry so that our general statements (based on symmetry arguments[21]) should also hold if strain effects were more realistically included. Here we take into account only the strain-induced piezoelectric field in the structure, as described in the following section.

A. The electrostatic built-in field

For the nitride based heterostructures the electrostatic built-in field plays an important role and can significantly modify the electronic structure as well as the optical properties. In contrast to cubic III-V semiconductor heterostruc-

TABLE II. Parameters for lattice, piezoelectric e_{ij}, elastic C_{ij}, and spontaneous polarization P^{spont} constants for wurtzite InN and GaN, taken from Ref. 27.

	InN	GaN
a (Å)	3.545	3.189
c (Å)	5.703	5.185
e_{31} (C/m^2)	−0.23	−0.20
e_{33} (C/m^2)	0.39	0.29
C_{13} (GPa)	9.4	11.4
C_{33} (GPa)	20.0	38.1
P^{spont} (C/m^2)	−0.042	−0.034

tures, based on InAs or GaAs, the III-V nitrides exhibit considerably larger electrostatic built-in fields for several reasons.[55] First of all the shape of the unit cell in InN and GaN differs slightly from the ideal symmetry in the wurtzite structure. This small aberration causes a polarization, which is referred to as the spontaneous polarization $\mathbf{P}^{\text{spont}}$. Additionally, a strain-induced piezoelectric field occurs that is quite strong in InN/GaN heterostructures, compared, for example, with cubic GaAs-based structures. Being different as for the zinc-blende structure the piezoelectric tensor of the wurtzite structure has three nonvanishing independent components,[56] which are several times larger than the values for other group-III-V binary compounds, and which determine the magnitude of the piezoelectric field.[55]

The electrostatic potential ϕ_p is determined by solution of the Poisson equation as outlined in the following. We start from the Maxwell equation $\text{div}\,\mathbf{D}=0$ for the displacement field $\mathbf{D}$, which is defined by

$$\mathbf{D} = \epsilon_0\epsilon_r\mathbf{E} + (\mathbf{P}^{\text{spont}} + \mathbf{P}^{\text{piezo}}) = \epsilon_0\epsilon_r\mathbf{E} + \mathbf{P}, \tag{4}$$

where ϵ_r is the dielectric constant, $\mathbf{P}^{\text{spont}}$ and $\mathbf{P}^{\text{piezo}}$ are the spontaneous and strain-induced polarization, respectively. The spontaneous polarization $\mathbf{P}^{\text{spont}}$ in the wurtzite crystal structure lies within growth direction: $\mathbf{P}^{\text{spont}}=P^{\text{spont}}\mathbf{e}_z$. The strain contribution $\mathbf{P}^{\text{piezo}}$ to the polarization $\mathbf{P}$ is approximated as described in Ref. 57, $\mathbf{P}^{\text{piezo}}\sim\mathbf{e}_z$, with the lattice, elastic, piezoelectric, and dielectric constants from Ref. 27 as summarized in Table II. For InN and GaN several different values have been reported for these material parameters in the literature. The relatively large variation is dominantly caused by the fact that it is difficult to grow sufficiently large bulk crystals,[58,59] but also by the different defect situation in every single sample. An overview and a discussion of the influence of different piezoelectric and elastic constants on the internal field of InN and GaN is given in Ref. 60. In our calculations, a different value for the built-in field would yield an overall shift in the one-particle energy levels, especially for the hole states. However, even with different values for the built-in field a similar qualitative behavior especially of the ordering of the one-particle states and its dependence on the QD size can be expected as it has already been observed for different material systems before.[28] For our chosen QD geometry, a more sophisticated inclusion of strain effects[22] will generate merely small lateral contributions to the piezoelectric field,[61] which are therefore neglected in the following. Furthermore, the small thermal strain contribution is neglected.[57,62] From the knowledge of the polarization $\mathbf{P}$ the charge density ρ_p and the electrostatic potential ϕ_p can be obtained,

$$\text{div}\,\mathbf{P} = -\rho_p. \tag{5}$$

Assuming only small contributions from image charges, the electrostatic potential ϕ_p is given by

$$\Delta\phi_p = -\frac{1}{\epsilon_0\epsilon_r}\rho_p. \tag{6}$$

The resulting electrostatic potential is included in the TB model as a site-diagonal potential energy $V_p(\mathbf{r})=-e_0\phi_p(\mathbf{r})$. This method has been successfully applied to quantum well[63] and QD[61] structures before. With the electrostatic energy V_p, a rough estimate for the electrostatic field strength of about 5.5 MV/cm inside the QD can be obtained from a simple capacitor model.

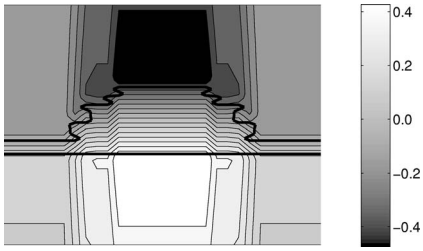

FIG. 3. Contour plot of the electrostatic potential energy V_p. A slice in the x-z plane through the center of the QD is depicted. The result is shown for the smallest QD but is qualitatively the same for all the investigated QD sizes.

A contour plot of the electrostatic potential energy V_p is shown in Fig. 3 for the smallest QD. A representative picture is given because the potential inside the QD looks qualitatively the same for all the investigated QD sizes. Outside the QD, a typical dependence of the potential is reproduced as known from QW systems. To reach convergence, the calculation of the built-in field, according to Eqs. (5) and (6), is performed on a much larger area surrounding the QD-WL structure, so that the field vanishes at the supercell boundaries in z direction.

B. One-particle properties

Figure 4 shows the QD geometry and the first three bound one-particle states for the largest QD for electrons and holes, respectively, including the influence of the built-in field. For each state the atomic orbital character of the TB wave functions is given where the dominant contributions are highlighted. According to their nodal structure, the depicted electron states $\psi^e_{1,2,3}$ can be classified as s- and p-like states. This classification is not possible for the hole states; these states underly a strong band mixing. Whereas only one of the p-like valence bands may contribute to the formation of the bound states (two-dimensional bands) in the case of QW systems,[16] at least two atomic p states contribute to the formation of the QD hole states. Therefore the assumption of a

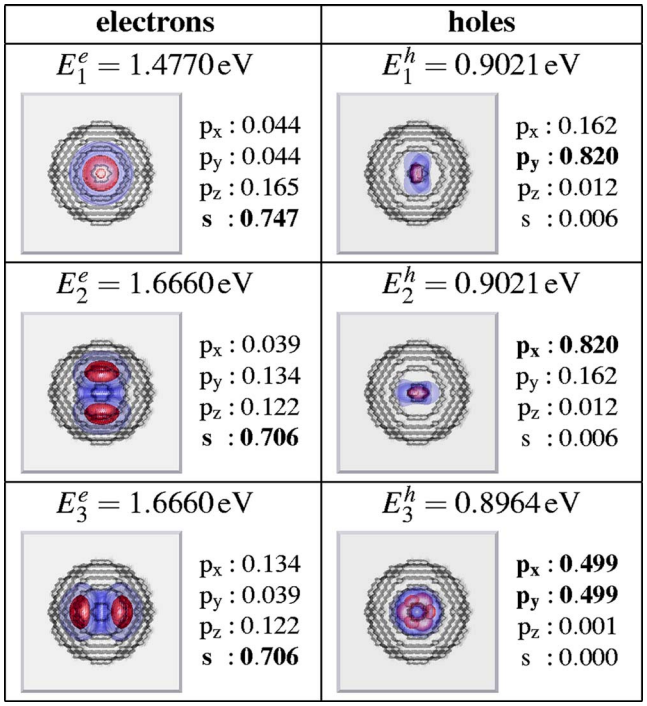

FIG. 4. (Color online) The QD geometry is shown for the largest QD from atop. The structure is visualized and isosurfaces of the probability density for the three lowest electron (left) and hole (right) states with built-in field are included for 10% (blue) and 50% (red) of the maximum value. The atomistic structure and the C_{3v} symmetry of the wurtzite crystal becomes most apparent for the hole states. The corresponding energies ($E^{e,h}_{1,2,3}$) of electron and hole states, measured from the valence band maximum of bulk GaN, and the atomic orbital character for each wave function are given. The dominant contributions are highlighted.

single heavy-hole valence band for the description of the bound hole states in a QD even qualitatively yields incorrect results. The observation of strong band-mixing effects for the bound hole states is in agreement with results from other multiband approaches.[40,54] The one-particle states obtained from our TB treatment agree qualitatively very well with recent $k\cdot p$ calculations for truncated hexagonal pyramidal GaN/AlN QDs with a wurtzite structure,[21,54] although in these references the strain is modeled on a microscopic level. Therefore, we expect that our general statements in this work, based on symmetry arguments, should also hold if strain effects were microscopically included in our model.

According to their degeneracy and their transformation properties under rotation by $2\pi/3$, electron as well as hole states are classified as s and p states. The two energetically degenerate states are denoted as p states, while the single degenerate state is the s state. For convenience, here, we choose real-valued wave functions $\psi_{p_{x,y}}$ for the two degenerate p states of electrons and holes, respectively. However, by choosing appropriate linear combinations $\psi_{p_\pm} = \mp(1/\sqrt{2}) \times (\psi_{p_x} \pm i\psi_{p_y})$ they can be transformed into states which have the following properties under rotation by $2\pi/3$ around the z axis, $R_{2\pi/3}\psi_{p_\pm} = e^{\pm i(2\pi/3)}\psi_{p_\pm}$, according to the system symmetry. These states are complex-valued but are favorable for the discussion of certain properties of the Coulomb matrix elements[34] as done in Sec. IV A.

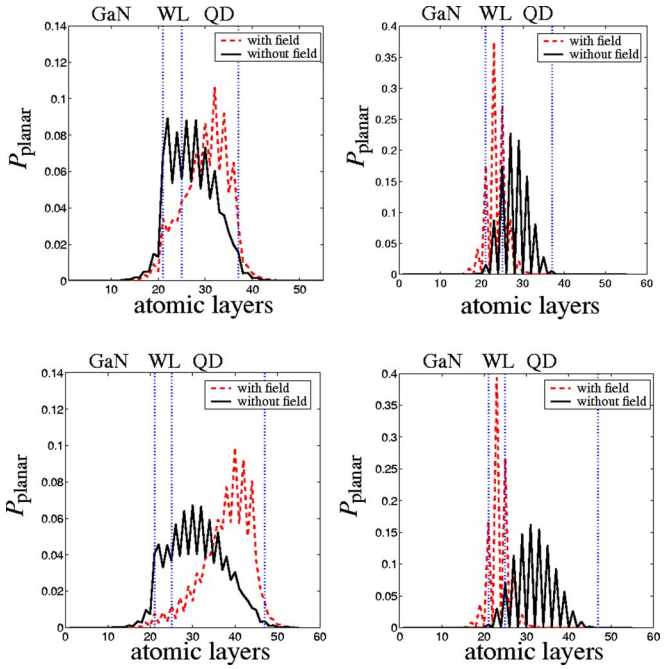

FIG. 5. (Color online) Planar-integrated probability density P_{planar} for the electron (left) and the hole (right) ground state, without (solid lines) and with (dashed lines) built-in field for the smallest (top) and the largest (bottom) QD.

With inclusion of the built-in field, the electron states are squeezed into the cap of the QD, while the hole states are constraint to a few atomic layers at the bottom, near the wetting layer. This is illustrated in Fig. 5 for the planar-integrated electron ψ_1^e and hole ψ_1^h ground state probability density $P_{\mathrm{planar}} = \Sigma_{i,j}|\psi(x_i, y_i, z)|^2$ in the smallest and in the largest QD. The influence of the electrostatic field on the one-particle densities is much more pronounced for the larger QD. In this case a clear spatial separation of electron and hole probability densities is observed, which lowers the direct spatial overlap of electron and hole wave functions and leads to reduced (small) dipole matrix elements. Besides the influence on the oscillator strength, the additional confinement of the electrons into the cap of the QD increases the electronic Coulomb matrix elements.

The dependence of the energy spectrum on the QD size for the first five electron and first 10 hole one-particle states, including the built-in field, is shown in Fig. 6(a). All energies are measured relative to the valence-band maximum of GaN. The energies are compared with the ground state energies for electrons and holes in an InN-WL (WL_1^e and WL_1^h, respectively) of one lattice constant c thickness, which is calculated separately for the WL without the QD. As expected from a naive particle-in-a-box picture, the binding of the electrons and holes becomes stronger in the QD when the QD size is increased. For the intermediate and the largest QD, the hole ground state is formed by the twofold degenerate p states ψ_1^h and ψ_2^h. This behavior is interchanged with decreasing QD size where, for the smallest QD, the s state ψ_3^h becomes the hole ground state. This energy level-crossing with changing QD size is illustrated in terms of the energy eigenvalues in Fig. 6(b) and has been reported before for other QD

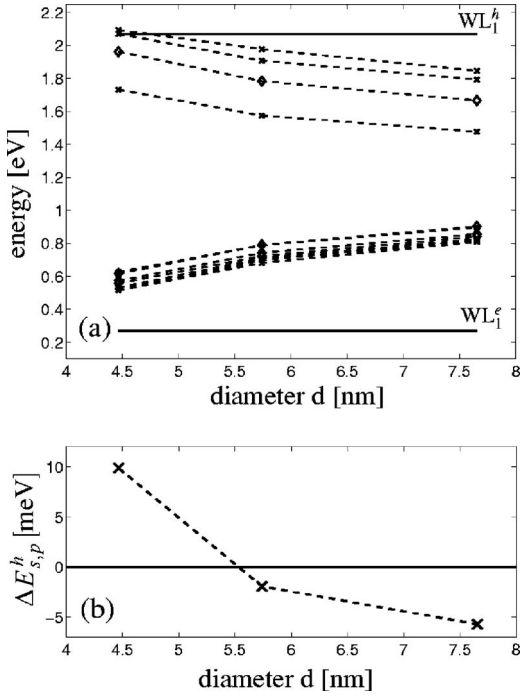

FIG. 6. (a) The first five electron and 10 hole one-particle energy levels are shown for the three investigated QD sizes with increasing diameter from left to right (the dashed lines are included as a guide to the eye). The results are shown with the influence of the built-in field. As a consequence of the stronger quantum confinement of the carriers inside the QD structure for decreasing size, a clear blueshift of the effective gap energy is observed. (b) The energy splitting $\Delta E^h_{s,p}=E^h_s-E^h_p$ between the s and the p shell for the holes is depicted. By definition the splitting is positive for the smallest QD and changes sign with increasing QD diameter d, where the twofold degenerate p shell constitutes the hole ground states (the dashed lines are included as a guide to the eye).

systems.[28] To concentrate on the level crossing of the first three bound hole states, Fig. 6(b) displays the energy splitting $\Delta E^h_{s,p}=E^h_s-E^h_p$ between the s and the p shell for the holes. By definition the splitting is positive for the smallest QD and changes sign with increasing QD diameter d.

To investigate the influence of the built-in field, we compare the energies of the first three bound electron $(\psi^e_1,\psi^e_{2,3})$ and hole states $(\psi^h_{1,2},\psi^h_3)$ with and without the electrostatic field. The results for the intermediate QD size are shown in Fig. 7. First of all, the electrostatic field shifts the electron single-particle states to lower energies, whereas the hole states are shifted to higher energies. Consequently, the built-in field leads to an overall redshift in the single-particle energy gap. Furthermore, the electrostatic field affects the ordering of the first three bound hole states. Without the electrostatic field the hole ground state is the nondegenerate state ψ^h_3 as for the largest QD in Fig. 4. The first two excited states ψ^h_1 and ψ^h_2 are degenerate. The electrostatic field interchanges the ordering of the states ψ^h_3 and $\psi^h_{1,2}$. In this case the hole ground state is twofold degenerate. For clarity, the splitting of 1.9 meV between ground and first excited state is displayed in the inset of Fig. 7. The ordering of the lowest hole states has strong implications for the ground state dipole

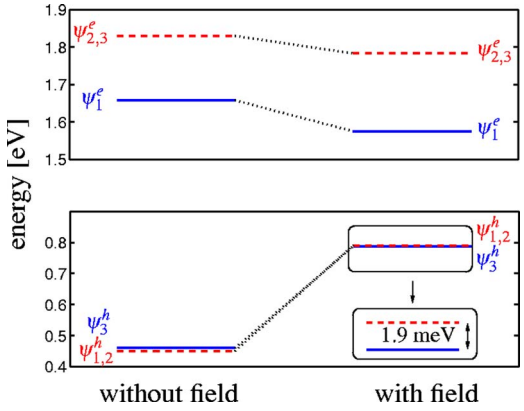

FIG. 7. (Color online) For the intermediate QD size the influence of the built-in field on the hole-state ordering is demonstrated. Without the electrostatic field the hole ground state is built by a single s-like state (solid line), whereas with the influence of the field the twofold degenerate p state (dashed line) constitutes the ground state for the holes. The dotted lines are included as a guide to the eye.

selection rules and therefore for the optical properties of the system.[28]

IV. MATRIX ELEMENTS

As emphasized above, a TB model represents an atomistic approach to describe the electronic structure of low-dimensional heterostructures. However, explicit knowledge about a basis set of localized states (atomic orbitals) is not required for the calculation of one-particle energies and wave functions. Orthogonal empirical TB models are based upon a basis set of states well localized at the atomic sites of the crystal. Only the basic assumptions about these localized orbitals, i.e., symmetry, spatial orientation,[39] and orthogonality, enter the TB Hamiltonian.

With the TB Hamiltonian one-particle states can be determined for electrons and holes which are localized in a semiconductor nanostructure. However, being interested in optical properties of the system, one-particle energies and wave functions are not sufficient. To study optical interband transitions, the calculation of dipole matrix elements between electron and hole wave functions and the calculation of Coulomb matrix elements is required. Besides the calculation of optical properties, the Coulomb matrix elements are of particular importance to study carrier-carrier[64] and carrier-phonon[65] scattering in InN/GaN QDs. For the calculation of these matrix elements one needs—in principle—the localized atomic basis states $\phi_{\alpha\mathbf{R}}(\mathbf{r})$ from which the one-particle eigenstates $\psi_i(\mathbf{r})$ are formed according to Eq. (2). In the following we describe how Coulomb and dipole matrix elements can be obtained within the empirical TB model.

A. Coulomb matrix elements

For the calculation of optical spectra, Coulomb matrix elements between the TB wave functions, Eq. (2), are required, which are given by

$$V_{ijkl} = \sum_{\mathbf{R}_1\mathbf{R}_2\mathbf{R}_3\mathbf{R}_4} \sum_{\alpha\beta\gamma\delta} c^{i*}_{\mathbf{R}_1\alpha} c^{j*}_{\mathbf{R}_2\beta} c^{k}_{\mathbf{R}_3\gamma} c^{l}_{\mathbf{R}_4\delta} \times \int d^3r d^3r' V(\mathbf{r}-\mathbf{r}') \phi^*_{\alpha\mathbf{R}_1}(\mathbf{r}) \phi^*_{\beta\mathbf{R}_2}(\mathbf{r}') \phi_{\gamma\mathbf{R}_3}(\mathbf{r}') \phi_{\delta\mathbf{R}_4}(\mathbf{r}), \tag{7}$$

$$\text{with } V(\mathbf{r}-\mathbf{r}') = \frac{e_0^2}{4\pi\varepsilon_0\varepsilon_r|\mathbf{r}-\mathbf{r}'|},$$

where e_0 denotes the electron charge, ε_0 the vacuum dielectric constant, and ε_r the background dielectric constant of the semiconductor material. As the atomic orbitals $\phi_{\alpha\mathbf{R}}(\mathbf{r})$ are not explicitly known in an empirical TB treatment, we approximate these matrix elements by

$$V_{ijkl} = \sum_{\mathbf{R}\mathbf{R}'} \sum_{\alpha\beta} c^{i*}_{\mathbf{R}\alpha} c^{j*}_{\mathbf{R}'\beta} c^{k}_{\mathbf{R}'\beta} c^{l}_{\mathbf{R}\alpha} V(\mathbf{R}-\mathbf{R}'), \tag{8}$$

with

$$V(\mathbf{R}-\mathbf{R}') = \frac{e_0^2}{4\pi\varepsilon_0\varepsilon_r|\mathbf{R}-\mathbf{R}'|} \quad \text{for } \mathbf{R} \neq \mathbf{R}'$$

and

$$V(0) = \frac{1}{V_{uc}^2} \int_{uc} d^3r d^3r' \frac{e_0^2}{4\pi\varepsilon_0\varepsilon_r|\mathbf{r}-\mathbf{r}'|} \approx V_0. \tag{9}$$

The validity of the underlying approximations and assumptions is discussed in Appendix A. Physically this means that the variation of the Coulomb interaction is taken into account only on a larger length scale of the magnitude of lattice vectors but not within one unit cell, which is justified because of the long ranged, slowly varying behavior of the Coulomb interaction. For $|\mathbf{R}-\mathbf{R}'|=0$ the evaluation of the integral in Eq. (9) can be done quasianalytically by expansion of the Coulomb interaction in terms of spherical harmonics following Ref. 66. An approximation like that leading to Eq. (8) is always made in the frequently used effective mass description of QDs, because only the spatial variation of the envelope function and no variation of the wave functions within an atomic unit cell is considered there. As shown in Appendix A, the approximations and assumptions leading to Eqs. (8) and (9) can be justified as long as $|\mathbf{R}-\mathbf{R}'|$ is larger than nearest-neighbor lattice vectors. Though the on-site and nearest-neighbor terms are absolutely the largest ones, their relative contribution to the double sum in Eq. (8) is less than 5%, because of which possible errors in the true values of the nearest-neighbor terms are only of minor importance for the total matrix elements V_{ijkl} between the QD states.

For our QD system the bound states are almost completely localized inside the InN material. Therefore in a good approximation we use the InN dielectric constant $\varepsilon_r=8.4$, taken from Ref. 27. For the calculation of Coulomb matrix elements averaged lattice constants are used to determine $\mathbf{R}-\mathbf{R}'$ in the whole structure, calculated from the unstrained InN and GaN lattice constants in Table II. Therefore, we take into account that in the vicinity of the QD, where the wave functions are localized, the InN structure is influenced by the surrounding GaN material and vice versa.

In the following, some basic results are summarized, regarding fundamental symmetry properties of the calculated Coulomb matrix elements. The discussion of Coulomb matrix elements is more convenient if the localized p states are chosen so that they are invariant under system rotation by $2\pi/3$ up to a phase factor $\exp(i2\pi/3\cdot m)$ as already introduced in Sec. III B. The integer m takes the values $m=\pm1$ for the p states and $m=0$ for the s state that is invariant under the rotation. For a system with full rotation invariance, as in effective mass approximation,[34] the integer m represents the quantum number of the z component of the electronic angular momentum in each state. For our system, a rotation by $2\pi/3$ transforms the Coulomb matrix elements according to

$$R_{2\pi/3} V_{ijkl} = e^{i(m_i+m_j-m_k-m_l)(2\pi/3)} V_{ijkl}. \tag{10}$$

As this rotation represents a symmetry operation for the chosen QD geometry and for the wurtzite lattice with discrete rotation invariance, the matrix elements must remain unchanged. Therefore $(m_i+m_j-m_k-m_l)$ mod $3=0$ must be fulfilled, otherwise the matrix element V_{ijkl} must vanish. This is different than in effective mass approximation where, for circular QD geometry, each rotation is a valid symmetry transformation, and where the angular momentum conservation requires $m_i+m_j-m_k-m_l=0$. Therefore, in our case all matrix elements with $(m_i+m_j-m_k-m_l)$ mod $3=0$ are, in principle, nonvanishing. However, the matrix elements that occur in addition to the result of the effective mass approximation are small compared to the matrix elements that simply fulfill $m_i+m_j-m_k-m_l=0$. They become even smaller for the larger QDs, where one comes closer to the case of full rotation invariance, because the influence of the underlying crystal lattice becomes less important.

Although the influence of the discrete rotation invariance still allows energetic degeneracy in the p shell, differences compared to continuumlike models are found here on the level of Coulomb matrix elements between the localized states. Although this feature becomes less important for the larger QD, the aspects of band mixing, present in the multiband formulation remain equally important, even for larger QDs. This becomes apparent in the next sections where the dipole matrix elements and selection rules are discussed in detail.

B. Dipole matrix elements

In general it is not a trivial task to incorporate electromagnetic fields into tight-binding models, but one must pay attention that gauge invariance, conservation laws, and sum rules remain valid. In particular in connection with the problem of lattice electrons in a magnetic field and the Peierls substitution[68,69] it has been pointed out that a vector potential describing the magnetic field must be included via complex, position-dependent phase factors of the intersite (hopping) TB matrix elements.[70–74] It has been emphasized[75] that this is the proper, unambiguous and gauge invariant way to incorporate arbitrary electromagnetic fields in the TB Hamil-

TABLE III. Slater orbitals for In, Ga, and N atoms. The radial part of the wave functions is given by $R(r)=r^a e^{-br}$. The constants a and b are given by Slater's rules (Ref. 67). The angular part is given by the spherical harmonics $Y_{lm}(\varphi,\vartheta)$.

Orbital α	In	Ga	N
s	$0.31r^3e^{-1.25r}Y_{00}$	$0.61r^{2.7}e^{-1.35r}Y_{00}$	$6.13r^1e^{-1.95r}Y_{00}$
p_x	$0.31r^3e^{-1.25r}\frac{-1}{\sqrt{2}}(Y_{11}-Y_{1-1})$	$0.61r^{2.7}e^{-1.35r}\frac{-1}{\sqrt{2}}(Y_{11}-Y_{1-1})$	$6.13r^1e^{-1.95r}\frac{-1}{\sqrt{2}}(Y_{11}-Y_{1-1})$
p_y	$0.31r^3e^{-1.25r}\frac{i}{\sqrt{2}}(Y_{11}+Y_{1-1})$	$0.61r^{2.7}e^{-1.35r}\frac{i}{\sqrt{2}}(Y_{11}+Y_{1-1})$	$6.13r^1e^{-1.95r}\frac{i}{\sqrt{2}}(Y_{11}+Y_{1-1})$
p_z	$0.31r^3e^{-1.25r}Y_{10}$	$0.61r^{2.7}e^{-1.35r}Y_{10}$	$6.13r^1e^{-1.95r}Y_{11}$

tonian. However, when studying weak optical fields with only a slight position dependence on the scale of lattice vectors, a description of the field only via a scalar potential is possible. Then at least in linear order in the field also the expansion of the matrix elements of the gauge invariant TB model leads back to a coupling of the field via the dipole operator, as it is nearly always used in the standard effective-mass models of semiconductor physics (optics). Therefore, here we use this simplifying assumption, too. Then the task is the calculation of the matrix elements of the dipole operator $e_0\mathbf{r}$ with the TB wave functions $\mathbf{d}_{ij}^{eh}=e_0\langle\psi_i^e|\mathbf{r}|\psi_j^h\rangle$, which yield information on selection rules, allowed and forbidden transitions, and even relative peak heights, at least qualitatively.[76]

Following the discussion of the preceding paragraph, for the calculation of optical spectra the dipole matrix elements between electron and hole wave functions are an essential ingredient. In contrast to the Coulomb matrix elements, the short-range contributions dominate dipole matrix elements. This short-range, almost local, character of the dipole operator in real space is in accordance with the assumption of a weak $\mathbf{k}$ dependence of the dipole matrix elements,[77] which is commonly used in connection with effective-mass approaches.[78] Therefore, what turns out to be a good approximation for the Coulomb matrix elements, to neglect the precise structure of the localized orbitals, fails for the calculation of dipole matrix elements.

In accordance with the TB formulation, the position operator can be decomposed into two contributions:[32,76,79]

$$\mathbf{r}=\sum_{\mathbf{R}\alpha}|\mathbf{R},\alpha\rangle\mathbf{R}\langle\mathbf{R},\alpha|+\sum_{\mathbf{R}\alpha}\sum_{\mathbf{R}'\beta}|\mathbf{R}\alpha\rangle\langle\mathbf{R}\alpha|\tilde{\mathbf{r}}|\mathbf{R}'\beta\rangle\langle\mathbf{R}'\beta|. \tag{11}$$

Here, $\mathbf{R}=(X,Y,Z)$ and $\mathbf{R}'=(X',Y',Z')$ denote the discrete atomic positions and $\tilde{\mathbf{r}}=\mathbf{r}-\mathbf{R}=(\tilde{x},\tilde{y},\tilde{z})$ is the position within a unit cell relative to $\mathbf{R}$. The indices α,β label the different atomic orbitals. An optical light pulse is considered, with light polarization vector $\mathbf{e}=1/\sqrt{2}(1,1,0)$. With the decomposition, Eq. (11), and the TB wave functions, Eq. (2), the dipole matrix elements $d_{ij}^{eh}=\mathbf{e}\mathbf{d}_{ij}^{eh}$ then explicitly read

$$d_{ij}^{eh}=\frac{e_0}{\sqrt{2}}\sum_{\mathbf{R}\mathbf{R}'\alpha\beta}c_{\mathbf{R},\alpha}^{i,e*}c_{\mathbf{R}',\beta}^{j,h}[(X+Y)\delta_{\mathbf{R}\mathbf{R}'}\delta_{\alpha\beta}+\langle\mathbf{R},\alpha|\tilde{x}+\tilde{y}|\mathbf{R}',\beta\rangle]. \tag{12}$$

The first part in Eq. (12) is the contribution to the dipole matrix elements which stems from the TB coefficients ("envelope") which are weighted with the position of the corresponding atom site. The second part contains the matrix elements of the operator $\tilde{\mathbf{r}}$ with the localized (atomic) basis orbitals $\phi_{\alpha\mathbf{R}}(\mathbf{r})$ and is determined by their variation inside the unit cell.

In the literature a variety of different approximations for the calculation of the matrix elements in Eq. (12) has been applied in the past.[16,32,79–83] In some of this work, the first part, the envelope part, has been neglected,[16,83] whereas in other works parts of the second contribution, the orbital contribution, have been included in addition to the envelope contribution.[32,79,82] However, no general statement has been made, which part is the dominant one for which kind of system. To give a representative picture, at least for the investigated InN/GaN quantum dot system, here we include and discuss in detail both, orbital and envelope contribution.

The first part, the envelope part, can easily be calculated from our TB wave functions as a discrete sum over all lattice sites. The result does not depend on the choice of the origin. The proper calculation of the second part, the orbital contribution, is much more involved, which is the reason why in the available literature several different approximations and assumptions have been proposed.[16,32,79,80,82,83]

In the case of the orbital part it is necessary to connect the calculated TB coefficients $c_{\mathbf{R}\alpha}^i$ directly to the underlying set of atomic basis orbitals. A commonly used approach is the use of atomic Slater orbitals,[67] as given in Table III for In, Ga, N, which take into account the influence of the effective screening of inner electron densities on the effective one-particle wave functions for the bonding orbitals. These basis orbitals have been used in the past for the calculation of dipole matrix elements.[31,32] However, previous approaches contain two shortcomings which we have improved in our calculations.

(i) While they include the correct symmetry properties underlying the TB coefficients, the Slater orbitals lack the essential assumption of orthogonality with respect to different lattice sites, since they have been developed for isolated atoms. To overcome this problem, we use numerically orthogonalized Slater orbitals, as outlined in Appendix B. Including the orthogonality, the Slater orbitals fulfill all basic requirements, regarding symmetry, locality, and orthogonality for the basis orbitals underlying the TB formulation.

(ii) In most approaches only on-site contributions to the dipole matrix elements have been included,[16,17,32,79] which results in a local dipole interaction where only the direct

overlap of electron and hole wave functions is taken into account for the calculation of these matrix elements. To properly treat the slight nonlocality of the dipole operator[80,82] and in particular the anion-cation structure of the crystal, the matrix elements are calculated including up to second-nearest neighbors here.

In the past, even nearest-neighbor contributions have been neglected, because the matrix elements $\langle \mathbf{R}, \alpha | \tilde{x} + \tilde{y} | \mathbf{R}', \beta \rangle$ (with $\mathbf{R}$ and $\mathbf{R}'$ being neighboring atom sites) are much smaller than the corresponding on-site contributions (with $\mathbf{R}=\mathbf{R}'$). However, in Eq. (12) not only the matrix elements alone determine the result but they are also weighted with the TB coefficients of electron, $c^{i,e}_{\mathbf{R},\alpha}$, and hole, $c^{j,h}_{\mathbf{R}',\beta}$, wave function. From an intuitive picture, having in mind the anion-cation-structure of the crystal, one might guess, that the product of the TB coefficients $c^{i,e}_{\mathbf{R},\alpha} \cdot c^{j,h}_{\mathbf{R}',\beta}$ is larger for $\mathbf{R},\mathbf{R}'$ labeling nearest-neighbor atom sites than for $\mathbf{R}=\mathbf{R}'$. As has been visualized in Fig. 5 before, the main contributions to electron and hole wavefunctions are localized at different kinds of atoms, and therefore different layers in the crystal, electrons at the cations and holes at the anions. Therefore it can hardly be estimated in advance which contributions will be large and which small. Furthermore, the angular momentum selection rules,[16] which are valid for the on-site matrix elements in a good approximation cannot be used for transitions between orbitals which are centered around different lattice sites.

In order to rigorously estimate the influence of the different matrix elements and in order to give further insight into the nonlocal behavior of the dipole operator we will discuss the orbital contributions in detail in the following before we present the final results for the dipole matrix elements.

In contrast to previous approaches all the orbital contributions have been numerically calculated. To verify the numerical calculation of dipole matrix elements between the localized atomic orbitals, it can be checked in comparison to the quasianalytical results which can be obtained for the on-site contributions with standard Slater orbitals, without orthogonalization.[32] Matrix elements with a numerical error smaller than 1% can easily be obtained by choosing a sufficiently fine grid of quadrature points for the numerical evaluation of integrals.

We do not tabulate all the dipole matrix elements but prefer to summarize some general statements, valid for the orbital contributions to all the calculated matrix elements between the electron and hole TB wave functions. For the on-site contributions the calculations with orthogonalized and original Slater orbitals yield similar results with up to 8% difference. This finding demonstrates that the orthogonalized orbitals are still dominated by their original character in the vicinity of the origin, see Appendix B. Without orthogonalization the nearest- and second-nearest-neighbor contributions are strongly overestimated compared to the results of the orthogonalized orbitals. With orthogonalization, the main nonlocal contribution to the dipole matrix elements stems from the nearest neighbors. The second nearest neighbors are much less important and contribute by about 5% of the on-site contributions, which is in accordance with the TB formulation where nearest-neighbor hopping is included but hopping to more distant neighbors can be neglected in a good approximation.

Our results clearly demonstrate the short-range character of the dipole operator. However, despite its short-range character, it is essential to include the nearest-neighbor contributions to properly account for the anion-cation structure of the crystal lattice. In contrast to previous approaches all the nonlocal contributions have numerically been calculated here to avoid assumptions about angular momentum selection rules, which are strictly valid only for on-site contributions but which have been extended to nearest-neighbor contributions in earlier approaches.[80,82] The previously used assumptions for nonvanishing nearest-neighbor matrix elements, $\mathbf{d} \sim \mathbf{e}_z$, are not reproduced by our numerical results. Otherwise there would be no contribution from nearest neighbors for the light polarization $\mathbf{e}=1/\sqrt{2}(1,1,0)$ investigated here.

In the preceding paragraphs we have outlined how to bridge the gap between the TB coefficients of the empirical TB formulation and atomic basis orbitals, which allows to calculate the orbital contribution to the dipole matrix elements in addition to the envelope contribution. For the investigated system the envelope contribution is found to clearly dominate the total results for the dipole matrix elements, the orbital contributions are by about a factor of 30 smaller. However, this may change in other systems or for intraband transitions,[81] where the orbital contribution becomes more important. The dipole selection rules, which will be discussed in the next section, are the same for both contributions, only small differences for the ratio of different nonvanishing matrix elements are found for orbital and envelope contributions.

C. Dipole selection rules

The only relevant dipole matrix elements in our system are $\mathbf{ed}^{eh}_{sp_x} = \mathbf{ed}^{eh}_{sp_y}$ and $\mathbf{ed}^{eh}_{p_x s} = \mathbf{ed}^{eh}_{p_y s}$, where $\mathbf{e}=1/\sqrt{2}(1,1,0)$ denotes the light polarization vector. All other matrix elements are negligible due to the overall symmetry of the connected one-particle states.[28,37,84] The resulting optical selection rules are in strong contrast to what is known from many other III-V and II-VI heterostructures and cannot be explained within a one-component effective-mass approach.[85] Commonly used dipole matrix elements are diagonal with respect to the envelope symmetry (angular momentum),[16,34] namely $d^{eh}_{ij} \sim \delta_{ij}$ with $i,j \in \{s, p_+, p_-\}$.

The strong band mixing in the valence band is responsible for the transformation properties of the bound hole states which strongly influences the dipole selection rules for interband transitions to the conduction band. In many other systems with different symmetry of the crystal lattice and strong spin-orbit coupling for the valence bands, the dipole operator becomes diagonal with respect to the envelope angular momentum as used in Refs. 34 and 16. The dipole selection rules are important for the interpretation of the excitonic spectra in the following section as already demonstrated in Ref. 36.

The dipole selection rules are, in principle, unaffected by the built-in electrostatic field. However, for the large QD the ordering of the lowest hole states is interchanged by the in-

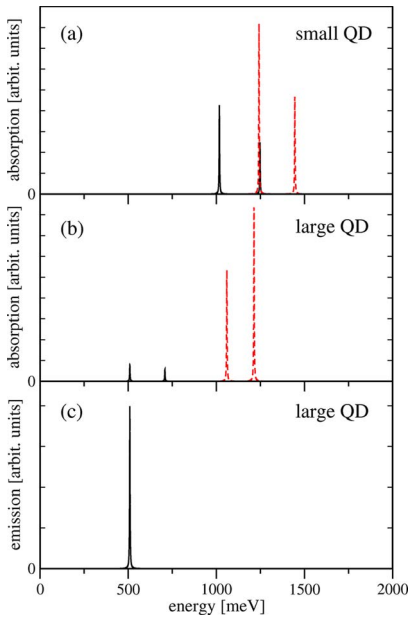

FIG. 8. (Color online) (a) Excitonic absorption for the small QD with (solid line) and without (dashed line) the influence of the built-in field. (b) Same as (a) but for the large QD. (c) Excitonic ground state emission for the large QD with the influence of the built-in field. Without the built-in field, the ground state emission vanishes and is consequently not shown.

fluence of the built-in field as already discussed in Sec. III B. This has strong implication on the optical emission spectra,[36] which will be discussed in the following section. Furthermore, the field-induced spatial electron-hole charge separation reduces the oscillator strengths drastically, by about a factor of 2 for the smallest QD, and by more than one order of magnitude for the largest QD.

V. EXCITONIC SPECTRA

Having calculated dipole and Coulomb matrix elements in the preceding sections, the calculation of excitonic absorption spectra in this section can directly be performed starting from the many-particle Hamiltonian in second quantization as given in, e.g., Ref. 34. For the localized states full configuration-interaction (FCI) calculations[11,34] are performed. Only bound states, *s* and *p* shell, are included in our calculation for electrons and holes, respectively, which can be justified by their energy separation to higher states in the structure and which keeps the following discussion simple and expressive. In Fig. 8 excitonic absorption and emission spectra, calculated with Fermi's golden rule,[34] are depicted for the smallest and the largest QD.

The excitonic absorption for the smallest QD is shown in Fig. 8(a) with (solid line) and without (dashed line) the influence of the built-in field. The two absorption lines in each spectrum correspond to the excitation of an exciton in the QD. In accordance with the FCI calculations, the lower energy line is dominated by contributions where the electron is excited in the *s* shell and the hole in the *p* shell, whereas the higher energy line mainly corresponds to the excitation of the hole in the *s* shell and the electron in the *p* shell. This is in accordance with the dipole selection rules discussed in the preceding section. The influence of the built-in field in the structure redshifts the whole excitonic spectrum by about 220 meV. The oscillator strengths are merely reduced by a factor of about 2. The strong confinement of the wave functions prevents a strong spatial separation of electron and hole wave functions as is the case for larger QDs. In addition to the redshift of the spectrum and the reduced oscillator strengths, the built-in field influences the Coulomb matrix elements, which, however, does not affect the optical spectra qualitatively. For the small QD no emission spectrum from the excitonic ground state is shown since no emission is observed in this case.[36] The excitonic ground state is dominated by a contribution where the electron is in the *s* shell as well as the hole. Since the dipole matrix element d_{ss}^{eh} vanishes, the interband transition from the *s* shell to the *s* shell is dipole forbidden, and the exciton ground state remains dark. The situation is the same with and without the built-in field.

For the large QD the excitonic absorption with (solid line) and without (dashed line) the built-in field is depicted in Fig. 8(b). As in the large QD the spatial separation of electron and hole wave functions is much larger, the redshift in energy and the reduction of the oscillator strengths (more than one order of magnitude) is much more pronounced than for the small QD. Furthermore, the relative oscillator strengths of the lines in the low-energy and the high-energy transitions is changed by the built-in field. As discussed in Sec. III B, the ground state for the holes in the large QD with the built-in field is a twofold degenerate *p* state. Therefore the ground state for the exciton in the large QD is dominated by the contribution where the electron is in the *s* shell and, this time, the hole is in the *p* shell. Therefore, in contrast to the small QD, for the large QD a nonvanishing exciton ground state emission can be observed, which is depicted in Fig. 8(c). No emission is observed without the built-in field.

The extension of the FCI calculation presented here to multiexciton spectra can be done with the same Coulomb and dipole matrix elements and has been presented in Ref. 36. The additionally required electron-electron and hole-hole Coulomb matrix elements can be calculated in complete analogy to the electron-hole matrix elements.

For the large QD, exciton ground state emission has been observed. However, the oscillator strength is drastically reduced by the field-induced spatial separation of electron and hole wave functions. Two possible solutions to avoid the strong reduction of the oscillator strength by the built-in field in the wurtzite structure have been discussed in the past: (1) growth along a non-polar axis in the crystal lattice,[30,86] (2) growth of smaller QDs. However, our results demonstrate that the growth of smaller QDs might turn out to have limitations concerning optical purposes. The small InN/GaN QD investigated here shows no exciton and no biexciton[36] ground state emission. Only for larger QDs the ground states become bright due to the influence of the built-in field.

VI. CONCLUSION

In conclusion, we successfully investigated the optical properties of InN/GaN QDs by means of an atomistic tight-

binding model. The wurtzite crystal structure of the underlying lattice is fully included in the formulation. Dipole and Coulomb matrix elements have been calculated which allow the investigation of excitonic absorption and emission spectra with microscopically determined input parameters. The calculations reveal strong influence of band-mixing effects on the optical transitions between the Coulomb correlated electron-hole states. The inclusion of the built-in field for the strained wurtzite crystal structure gives rise to a QCSE which creates a strong (about 220 meV for the small QD and about 600 meV for the large QD) redshift of the one-particle gap energy. Additionally, the Coulomb matrix elements are modified and the oscillator strengths are strongly reduced due to the spatial separation of electron and hole wave functions.

As an important consequence for future optoelectronic applications we predict vanishing exciton ground state emission for small lens-shaped InN/GaN QDs. For larger QDs we report bright ground state emission but with drastically reduced oscillator strengths caused by the QCSE.

ACKNOWLEDGMENTS

This work has been supported by the Deutsche Forschungsgemeinschaft (research group "Physics of nitride-based, nanostructured, light-emitting devices," project Cz 31/14-1,2). The authors also acknowledge a grant for CPU time from the NIC at the Forschungszentrum Jülich. Various valuable discussions with Paul Gartner, Norman Baer, and Frank Jahnke are gratefully acknowledged.

APPENDIX A: COULOMB MATRIX ELEMENTS

In this appendix we summarize the approximations that yield the Coulomb matrix elements in the form used in Eq. (8), and we point out in more detail on which assumptions these matrix elements are based. Furthermore, the quasianalytic calculation of the on-site matrix elements is briefly outlined. The discussion in this appendix is supposed to deepen the understanding of approaches to the Coulomb matrix elements in semiconductor quantum dots as already used in earlier works.[16]

Starting point is the Coulomb matrix element as given in Eq. (7),

$$V_{ijkl} = \sum_{\mathbf{R}_1\mathbf{R}_2\mathbf{R}_3\mathbf{R}_4} \sum_{\alpha\beta\gamma\delta} c^{i*}_{\mathbf{R}_1\alpha} c^{j*}_{\mathbf{R}_2\beta} c^{k}_{\mathbf{R}_3\gamma} c^{l}_{\mathbf{R}_4\delta} \cdot \int d^3r d^3r' V(\mathbf{r}-\mathbf{r}') \phi^*_{\mathbf{R}_1\alpha}(\mathbf{r}) \phi^*_{\mathbf{R}_2\beta}(\mathbf{r}') \phi_{\mathbf{R}_3\gamma}(\mathbf{r}') \phi_{\mathbf{R}_4\delta}(\mathbf{r}).$$

In principle, the Coulomb matrix elements involve four atomic orbitals $\phi_{\mathbf{R}\alpha}(\mathbf{r})$. According to Ref. 66 we take only two-center contributions into account. Off-site exchange integrals, with $\mathbf{R}_1=\mathbf{R}_3$ and $\mathbf{R}_2=\mathbf{R}_4$, decrease quickly as the distance between the atomic sites increases, due to the orthogonality and the localization of the atomic orbitals.[32] Therefore, terms with exchange character are also neglected. In this approximation, the Coulomb matrix elements are given by

$$V_{ijkl} \approx \sum_{\mathbf{R}\mathbf{R}'} \sum_{\alpha\beta\gamma a} c^{i*}_{\mathbf{R}\alpha} c^{j*}_{\mathbf{R}'\beta} c^{k}_{\mathbf{R}'\gamma} c^{l}_{\mathbf{R}\delta} \cdot \int_{\mathrm{uc}} d^3\tilde{r} d^3\tilde{r}' \frac{e_0^2 \phi^*_{\mathbf{R}\alpha}(\tilde{\mathbf{r}}) \phi^*_{\mathbf{R}'\beta}(\tilde{\mathbf{r}}') \phi_{\mathbf{R}'\gamma}(\tilde{\mathbf{r}}') \phi_{\mathbf{R}\delta}(\tilde{\mathbf{r}})}{4\pi\varepsilon_0\varepsilon_r |\mathbf{R}+\tilde{\mathbf{r}}-\mathbf{R}'-\tilde{\mathbf{r}}'|}.$$

We have decomposed the position operators $\mathbf{r}$ and $\mathbf{r}'$ into the positions $\mathbf{R}$ and $\mathbf{R}'$ of the lattice sites and the positions $\tilde{\mathbf{r}}$ and $\tilde{\mathbf{r}}'$ inside each unit cell. For sites which are far enough apart from each other the exact structure of the localized orbitals is not important. The long-range contributions are dominated by the monopole interaction of two charge densities localized at different lattice sites which leads to the approximation

$$V_{ijkl} \approx \sum_{\mathbf{R}\mathbf{R}'} \sum_{\alpha\beta\gamma a} c^{i*}_{\mathbf{R}\alpha} c^{j*}_{\mathbf{R}'\beta} c^{k}_{\mathbf{R}'\gamma} c^{l}_{\mathbf{R}\delta} V(\mathbf{R}-\mathbf{R}') \cdot \int d^3\tilde{r} \phi^*_{\mathbf{R}\alpha}(\tilde{\mathbf{r}}) \phi_{\mathbf{R}\delta}(\tilde{\mathbf{r}}) \int d^3\tilde{r}' \phi^*_{\mathbf{R}'\beta}(\tilde{\mathbf{r}}') \phi_{\mathbf{R}'\gamma}(\tilde{\mathbf{r}}').$$

Due to the orthogonality of the atomic orbitals, the final result for the Coulomb matrix elements is then given by

$$V_{ijkl} = \sum_{\mathbf{R}\mathbf{R}'} \sum_{\alpha\beta} c^{i*}_{\mathbf{R}\alpha} c^{j*}_{\mathbf{R}'\beta} c^{k}_{\mathbf{R}'\beta} c^{l}_{\mathbf{R}\alpha} V(\mathbf{R}-\mathbf{R}') = \sum_{\mathbf{R}\mathbf{R}'} \sum_{\alpha\beta} c^{i*}_{\mathbf{R}\alpha} c^{j*}_{\mathbf{R}'\beta} c^{k}_{\mathbf{R}'\beta} c^{l}_{\mathbf{R}\alpha} \frac{e_0^2}{4\pi\varepsilon_0\varepsilon_r |\mathbf{R}-\mathbf{R}'|}. \quad \text{(A1)}$$

The on-site contributions for $|\mathbf{R}-\mathbf{R}|=0$ can be calculated by integration of the Coulomb interaction over the volume of one unit cell:

$$V(0) = \frac{1}{V_{\mathrm{uc}}^2} \int_{\mathrm{uc}} d^3r d^3r' V(\mathbf{r}-\mathbf{r}'). \quad \text{(A2)}$$

As already mentioned in Sec. IV A, the evaluation of the integral (including the Coulomb singularity) can be done

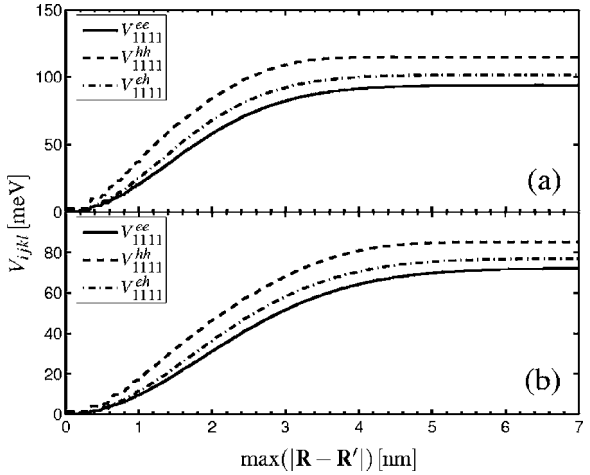

FIG. 9. Coulomb matrix elements calculated with a cutoff radius R_0 with $|\mathbf{R}-\mathbf{R}'|<R_0$ in the sum of Eq. (A1). Results are shown for the direct electron-electron (solid line), hole-hole (dashed line), and electron-hole (dashed-dotted line) Coulomb matrix elements for the ground state wave functions without the influence of the built-in field. (a) Small QD. (b) Large QD.

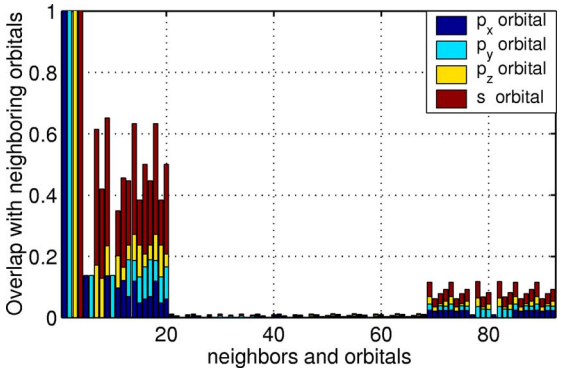

FIG. 10. (Color online) Overlap matrix $S_{\alpha\beta}^{0\mathbf{R}'}$ for a nitrogen atom to the atomic orbitals centered at the atom sites $\mathbf{R}'$ in the neighborhood up to third-nearest neighbors. The results are calculated with the original Slater orbitals. The overlap for the four different nitrogen orbitals $\alpha \in \{p_x, p_y, p_z, s\}$ is stacked in vertical direction and is visualized by the color coding. Contributions from different neighbors and their different orbitals β are given on the horizontal axis with increasing distance $|\mathbf{R}'|$ to the center nitrogen atom from left to right.

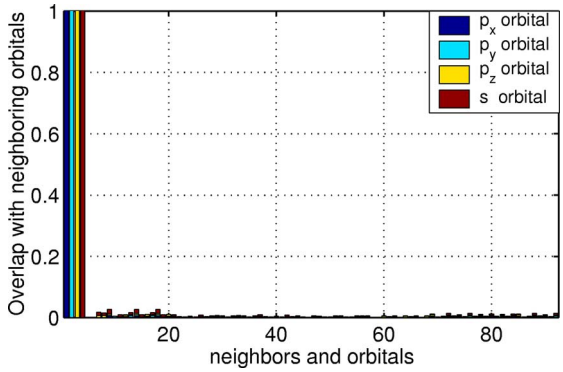

FIG. 11. (Color online) Same as Fig. 10 but calculated with the orthogonalized Slater orbitals.

quasianalytically by expansion of the Coulomb interaction in terms of spherical harmonics following the guidelines given in Ref. 66. The calculations yield meaningful values of about $\sim$16 eV for the unscreened on-site matrix elements. These values are in accordance with other calculations.[66] However, the exact values are not crucial for the QD Coulomb matrix elements since the screened on-site contributions are small compared to the long-range part.

The final result for the Coulomb matrix elements can be interpreted in an intuitive way as already outlined in Sec. IV A. In Eq. (A1) the atomic orbitals underlying the TB formulation do no longer enter the calculation of Coulomb matrix elements. Since the on-site and nearest-neighbor contributions—which are mostly affected by the above approximations—are small compared to the total Coulomb matrix elements, only small overall mistakes are made. Nearest-neighbor contributions are underestimated but only small additional contributions would apply to the long-range-dominated Coulomb matrix elements, at least for constant background screening, which is in accordance with the commonly used effective-mass approaches.[34]

For illustration purposes, in Fig. 9 results for the Coulomb interaction (A1) are shown which demonstrate that only rather minor contributions to the total matrix elements for our system originate from on-site and nearest-neighbor contributions. Results are depicted for the direct electron-electron, hole-hole, and electron-hole interaction in the smallest (upper panel) and the largest (lower panel) QD for the one-particle ground states without the influence of the built-in field. Similar results are found for all the investigated QD sizes as well as for the excited electron and hole states.

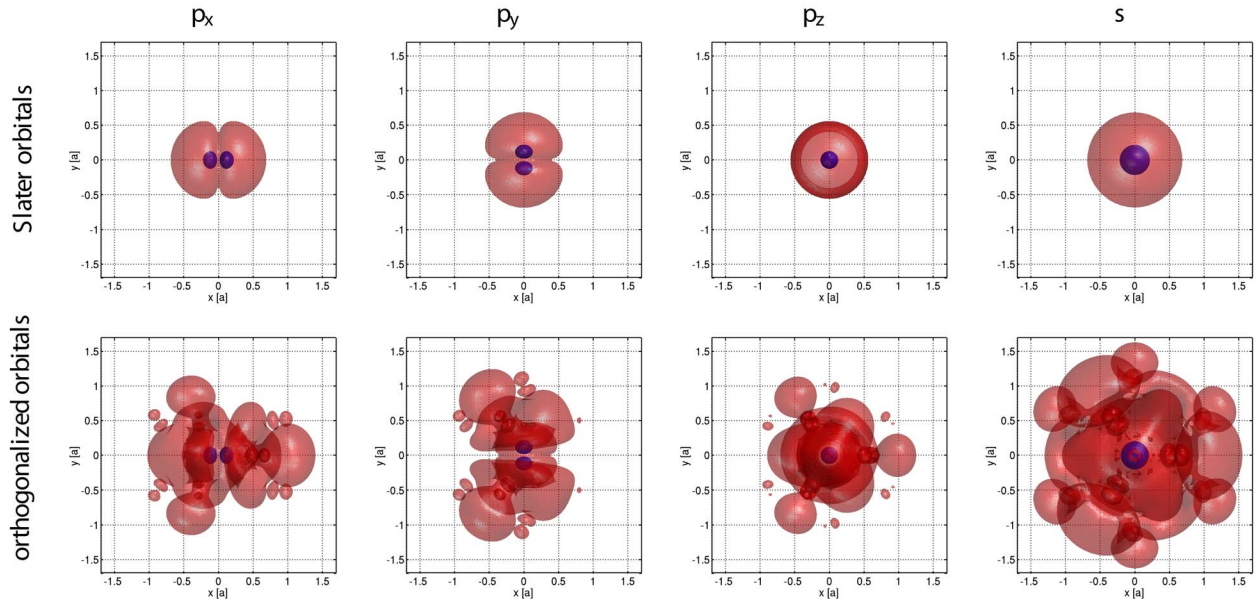

FIG. 12. (Color online) Nitrogen basis orbitals (Slater orbitals) without (top) and with (bottom) orthogonalization up to third-nearest neighbors. The depicted orbitals are from left to right: p_x, p_y, p_z, and s. The viewpoint is on the z axis. Two isosurfaces of the probability density are included with 20% (inner surface) and 0.001% (outer surface) of the maximum value, respectively.

The long-range part of the Coulomb interaction clearly dominates the results for which the treatment applied here can be justified. However, for different material systems or materials with an indirect band gap, results may change especially for the electron-hole exchange interaction[31] which has not been subject of this work.

APPENDIX B: ORTHOGONALIZED SLATER ORBITALS

In this appendix we give the details concerning the atomic basis orbitals $\phi_{\alpha\mathbf{R}}(\mathbf{r})$. They are required to calculate the optical dipole matrix elements with electron and hole wave functions $\psi_i(\mathbf{r})$ which are evaluated in terms of the empirical TB model. The overlap matrix of the atomic orbitals is given by

$$S_{\alpha\beta}^{\mathbf{R}\mathbf{R}'} = \langle \alpha, \mathbf{R} | \beta, \mathbf{R}' \rangle = \int d^3r \phi_\alpha^*(\mathbf{r}-\mathbf{R}) \phi_\beta(\mathbf{r}-\mathbf{R}'), \quad \text{(B1)}$$

with the position vectors $\mathbf{R}$, $\mathbf{R}'$ of the atoms at which the two orbitals $\alpha, \beta \in \{p_x, p_y, p_z, s\}$ are centered. For the original Slater orbitals, part of the overlap matrix, $S_{\alpha\beta}^{0\mathbf{R}'}$, is shown in Fig. 10 for a nitrogen atom in the origin $\mathbf{R}=0$ in an InN crystal structure. The overlap for the four different nitrogen orbitals $\alpha \in \{p_x, p_y, p_z, s\}$ with neighboring orbitals is stacked in the vertical direction and is visualized by the color coding. Contributions from different neighbors $\mathbf{R}'$ and their different orbitals β are given on the horizontal axis with increasing distance $|\mathbf{R}'|$ to the center nitrogen atom from left to right. The entries one to four on the horizontal axis show the overlap of the normalized orbitals with themselves, which is unity by definition. Contributions five to 20 correspond to the overlap to nearest neighbors (indium) with an averaged overlap of ≈ 0.427 for each neighboring orbital. The overlap 21 to 68 represents the overlap to second-nearest-neighbor (nitrogen) orbitals, with an averaged overlap of ≈ 0.008. Elements 69–92 give the overlap to third-nearest-neighbor (indium) orbitals, with an averaged overlap ≈ 0.081. Within an orthogonal basis this overlap matrix becomes the unit matrix which is a basic assumption for the TB model.

We apply a natural method to obtain an orthogonal set of atomic basis states which fulfill all the basic assumptions underlying the TB formulation in a good approximation. We start with the original Slater orbitals (given in Table III) localized at the atom sites in the wurzite crystal structure. The overlap matrix S is calculated for a finite neighborhood surrounding a central atom (here, up to third-nearest neighbors). The aim is to construct a set of orthogonal basis states for which the overlap matrix becomes the unit matrix $\mathbb{1}$, therefore we are looking for a transformation matrix X which fulfills $\mathbb{1}=X^\dagger S X$. One specific choice for the transformation matrix is obviously given by $X=S^{-1/2}$. The *non-unitary* transformation matrix X which transforms the overlap matrix S into a unit matrix is obtained by $X=S^{-1/2}=Ts^{-1/2}T^\dagger$. Here T is the unitary transformation matrix which brings S into diagonal form $s=T^\dagger S T$. The new (orthogonal) basis states C' are then obtained by the transformation $C'=XC$. This way, new basis orbitals are obtained which are centered around the atom in the center of the chosen neighborhood. The orthogonality to the new orbitals which are centered at atoms up to third nearest neighbors can be checked by calculation of the overlap matrix with the new orbitals as is visualized in Fig. 11 for the example of a nitrogen atom. The corresponding result without orthogonalization is shown in Fig. 10. The averaged overlap is reduced to ≈ 0.013 for nearest-neighbor orbitals, to ≈ 0.005 for second-nearest-neighbor orbitals, and to ≈ 0.009 for third-nearest-neighbor orbitals. Examples for the basis orbitals which are centered at a nitrogen atom in the crystal lattice are depicted in Fig. 12 without orthogonalization (top) and orthogonalization up to third-nearest neighbors (bottom). Two isosurfaces of the probability density are included with 20% (inner surface) and 0.001% (outer surface) of the maximum value, respectively. The sum of the nondiagonal overlap matrix elements is reduced by at least one order of magnitude for orthogonalization up to third-nearest neighbors. The figures, Figs. 10 and 11 demonstrate that the new basis states are orthogonal in a good approximation. Additionally, they mostly show the original symmetries of atomic orbitals which underly the TB Hamiltonian and are still rather well localized states at a certain atom site, Fig. 12. Only small contributions at the neighboring atom sites are found which are essential to obtain orthogonality. The added orthogonality now justifies the direct connection to the TB coefficients $c_{\mathbf{R}\alpha}^i$ since the orbitals fulfill all basic assumptions underlying an empirical TB model. Therefore the procedure demonstrated here to obtain an orthogonal set of atomic basis orbitals helps to improve earlier approaches for the calculation of optical properties from TB calculations.

[1] P. Michler, *Single Quantum Dots: Fundamentals, Applications, and New Concepts*, Topics in Applied Physics (Springer, Berlin, 2000).

[2] S. C. Jain, M. Willander, J. Narayan, and R. V. Overstraeten, J. Appl. Phys. **87**, 965 (2000).

[3] I. Vurgaftman and J. R. Meyer, J. Appl. Phys. **94**, 3675 (2003).

[4] J. Y. Marzin and G. Bastard, Solid State Commun. **92**, 437 (1994).

[5] M. Bayer, O. Stern, P. Hawrylak, S. Fafard, and A. Forchel, Nature (London) **405**, 923 (2000).

[6] O. Stier, M. Grundmann, and D. Bimberg, Phys. Rev. B **59**, 5688 (1999).

[7] R. Heitz, O. Stier, I. Mukhametzhanov, A. Madhukar, and D. Bimberg, Phys. Rev. B **62**, 11017 (2000).

[8] E. P. Pokatilov, V. A. Fonoberov, V. M. Fomin, and J. T. Devreese, Phys. Rev. B **64**, 245328 (2001).

[9] G. Bester and A. Zunger, Phys. Rev. B **71**, 045318 (2005).

[10] L.-W. Wang and A. Zunger, Phys. Rev. B **53**, 9579 (1995).

[11] A. Franceschetti, H. Fu, L. W. Wang, and A. Zunger, Phys. Rev. B **60**, 1819 (1999).

[12] G. Bester, S. Nair, and A. Zunger, Phys. Rev. B **67**, 161306(R) (2003).

[13] H. Dierks and G. Czycholl, J. Cryst. Growth **185**, 877 (1998).
[14] R. Santoprete, B. Koiller, R. B. Capaz, P. Kratzer, Q. K. K. Liu, and M. Scheffler, Phys. Rev. B **68**, 235311 (2003).
[15] S. Schulz and G. Czycholl, Phys. Rev. B **72**, 165317 (2005).
[16] W. Sheng, S. J. Cheng, and P. Hawrylak, Phys. Rev. B **71**, 035316 (2005).
[17] S. J. Sun and Y. C. Chang, Phys. Rev. B **62**, 13631 (2000).
[18] C.-N. Chen, Phys. Lett. A **329**, 136 (2004).
[19] S. L. Chuang, *Physics of Optoelectronic Devices*, Wiley series in pure and applied optics (Wiley-Interscience, New York, 1995).
[20] G. Khitrova, H. M. Gibbs, F. Jahnke, M. Kira, and S. W. Koch, Rev. Mod. Phys. **71**, 1591 (1999).
[21] A. D. Andreev and E. P. O'Reilly, Phys. Rev. B **62**, 15851 (2000).
[22] A. D. Andreev and E. P. O'Reilly, Appl. Phys. Lett. **79**, 521 (2001).
[23] M. Arlery, J. L. Rouviere, F. Widmann, B. Daudin, G. Feuillet, and H. Mariette, Appl. Phys. Lett. **74**, 3287 (1999).
[24] V. Chamard, T. Schulli, M. Sztucki, T. H. Metzger, E. Sarigiannidou, J.-L. Rouviere, M. Tolan, C. Adelmann, and B. Daudin, Phys. Rev. B **69**, 125327 (2004).
[25] F. Demangeot, J. Frandon, C. Pinquier, M. Caumont, O. Briot, B. Maleyre, S. Clur-Ruffenach, and B. Gil, Phys. Rev. B **68**, 245308 (2003).
[26] R. W. Martin and K. P. O'Donnell, Phys. Status Solidi B **216**, 441 (1999).
[27] J.-J. Shi and Z.-Z. Gan, J. Appl. Phys. **94**, 407 (2003).
[28] A. Bagga, P. K. Chattopadhyay, and S. Ghosh, Phys. Rev. B **71**, 115327 (2005).
[29] J. Simon, N. T. Pelekanos, C. Adelmann, E. Martinez-Guerrero, R. Andre, B. Daudin, L. S. Dang, and H. Mariette, Phys. Rev. B **68**, 035312 (2003).
[30] N. Garro, A. Cros, A. Cantarero, A. Vinattieri, M. Gurioli, S. Founta, H. Mariette, B. Daudin, and J. A. Budagosky, Appl. Phys. Lett. **87**, 011101 (2005).
[31] S. Lee, L. Jönsson, J. W. Wilkins, G. W. Bryant, and G. Klimeck, Phys. Rev. B **63**, 195318 (2001).
[32] S. Lee, J. Kim, L. Jönsson, J. W. Wilkins, G. W. Bryant, and G. Klimeck, Phys. Rev. B **66**, 235307 (2002).
[33] A. Barenco and M. A. Dupertuis, Phys. Rev. B **52**, 2766 (1995).
[34] N. Baer, P. Gartner, and F. Jahnke, Eur. Phys. J. B **42**, 231 (2004).
[35] S. M. Ulrich *et al.*, Phys. Rev. B **71**, 235328 (2005).
[36] N. Baer, S. Schulz, S. Schumacher, P. Gartner, G. Czycholl, and F. Jahnke, Appl. Phys. Lett. **87**, 231114 (2005).
[37] M. Nirmal, D. J. Norris, M. Kuno, M. G. Bawendi, A. L. Efros, and M. Rosen, Phys. Rev. Lett. **75**, 3728 (1995).
[38] A. Kobayashi, O. F. Sankey, S. M. Volz, and J. D. Dow, Phys. Rev. B **28**, 935 (1983).
[39] J. C. Slater and G. F. Koster, Phys. Rev. **94**, 1498 (1954).
[40] S.-H. Wei and A. Zunger, Appl. Phys. Lett. **69**, 2719 (1996).
[41] D. Fritsch, H. Schmidt, and M. Grundmann, Phys. Rev. B **69**, 165204 (2004).
[42] G. L. Zhao, D. Bagayoko, and T. D. Williams, Phys. Rev. B **60**, 1563 (1999).
[43] J. L. Birman, Phys. Rev. **115**, 1493 (1959).
[44] A. Kasic, M. Schubert, S. Einfeldt, D. Hommel, and T. E. Tiwald, Phys. Rev. B **62**, 7365 (2000).
[45] J. Wu, W. Walukiewicz, W. Shan, K. M. Yu, J. W. Ager III, E. E. Haller, H. Lu, and W. J. Schaff, Phys. Rev. B **66**, 201403(R) (2002).
[46] J.-M. Jancu, F. Bassani, F. D. Salla, and R. Scholz, Appl. Phys. Lett. **81**, 4838 (2002).
[47] S. Sapra and D. D. Sarma, Phys. Rev. B **69**, 125304 (2004).
[48] S. Schulz and G. Czycholl, Phys. Status Solidi C **3** 1675 (2006).
[49] C. G. Van de Walle and J. Neugebauer, Appl. Phys. Lett. **70**, 2577 (1997).
[50] G. Martin, A. Botchkarev, A. Rockett, and H. Morko, Appl. Phys. Lett. **68**, 2541 (1996).
[51] C. Manz, M. Kunzer, H. Obloh, A. Ramakrishnan, and U. Kaufmann, Appl. Phys. Lett. **74**, 3993 (1999).
[52] L. R. C. Fonseca, J. L. Jimenez, and J. P. Leburton, Phys. Rev. B **58**, 9955 (1998).
[53] M. A. Cusack, P. R. Briddon, and M. Jaros, Phys. Rev. B **54**, R2300 (1996).
[54] V. A. Fonoberov and A. A. Balandin, J. Appl. Phys. **94**, 7178 (2003).
[55] F. Bernardini, V. Fiorentini, and D. Vanderbilt, Phys. Rev. B **56**, R10024 (1997).
[56] V. A. Fonoberov and A. A. Balandin, J. Vac. Sci. Technol. B **22**, 2190 (2004).
[57] S. De Rinaldis, I. D'Amico, and F. Rossi, Phys. Rev. B **69**, 235316 (2004).
[58] B. Monema, P. P. Paskov, and A. Kasi, Superlattices Microstruct. **38**, 38 (2005).
[59] B. Monema, J. Cryst. Growth **189/190**, 1 (1998).
[60] U. M. E. Christmas, A. D. Andreev, and D. A. Faux, J. Appl. Phys. **98**, 073522 (2005).
[61] T. Saito and Y. Arakawa, Physica E (Amsterdam) **15**, 169 (2002).
[62] S. De Rinaldis, I. D'Amico, and F. Rossi, Appl. Phys. Lett. **81**, 4236 (2002).
[63] F. D. Sala, A. D. Carlo, P. Lugli, F. Bernardini, V. Fiorentini, R. Scholz, and J. M. Jancu, Appl. Phys. Lett. **74**, 2002 (1999).
[64] T. R. Nielsen, P. Gartner, M. Lorke, J. Seebeck, and F. Jahnke, Phys. Rev. B **72**, 235311 (2005).
[65] J. Seebeck, T. R. Nielsen, P. Gartner, and F. Jahnke, Eur. Phys. J. B **49**, 167 (2006).
[66] I. Schnell, G. Czycholl, and R. C. Albers, Phys. Rev. B **65**, 075103 (2002).
[67] J. C. Slater, Phys. Rev. **36**, 57 (1930).
[68] R. E. Peierls, Z. Phys. **80**, 763 (1933).
[69] J. M. Luttinger, Phys. Rev. **84**, 814 (1951).
[70] D. R. Hofstadter, Phys. Rev. B **14**, 2239 (1976).
[71] A. Rauh, G. H. Wannier, and G. Obermair, Phys. Status Solidi B **63**, 215 (1974).
[72] G. H. Wannier, Phys. Status Solidi B **70**, 727 (1975).
[73] G. M. Obermair and G. H. Wannier, Phys. Status Solidi B **76**, 217 (1976).
[74] G. Czycholl and W. Ponischowski, Z. Phys. B: Condens. Matter **73**, 343 (1988).
[75] M. Graf and P. Vogl, Phys. Rev. B **51**, 4940 (1995).
[76] G. W. Bryant and W. Jaskolski, Phys. Rev. B **67**, 205320 (2003).
[77] H. Haug and S. W. Koch, *Quantum Theory of the Optical and Electronic Properties of Semiconductors*, 3rd ed. (World Scientific, Singapore, 1995).
[78] S. Schumacher, G. Czycholl, F. Jahnke, I. Kudyk, L. Wischmeier, I. Rückmann, T. Voss, J. Gutowski, A. Gust, and D. Hommel, Phys. Rev. B **72**, 081308(R) (2005).
[79] K. Leung and K. B. Whaley, Phys. Rev. B **56**, 7455 (1997).
[80] K. Leung, S. Pokrant, and K. B. Whaley, Phys. Rev. B **57**, 12291

(1998).
[81] H. Jiang and J. Singh, IEEE J. Quantum Electron. **34**, 1188 (1998).
[82] J. Perez-Conde and A. K. Bhattacharjee, Phys. Rev. B **63**, 245318 (2001).
[83] J. G. Diaz, J. P. G. W. Bryant, and J. Aizpurua, J. Phys. Chem. B **108**, 17800 (2004).
[84] A. Bagga, P. K. Chattopadhyay, and S. Ghosh, Phys. Rev. B **68**, 155331 (2003).
[85] J. Li and J.-B. Xia, Phys. Rev. B **61**, 15880 (2000).
[86] S. Founta, F. Rol, E. Bellet-Amalric, J. Bleuse, B. Daudin, B. Gayral, H. Mariette, and C. Moisson, Appl. Phys. Lett. **86**, 171901 (2005).